Computational and Structural Biotechnology Journal 21 (2023) 4859–4867

Contents lists available at ScienceDirect

Computational and Structural Biotechnology Journal

journal homepage: www.elsevier.com/locate/csbj

Research article

Analyzing the contribution of vasa vasorum in oxygenation of the aneurysmal wall: A computational study

Alexis Throop, Manoela Neves, Rana Zakerzadeh *

Department of Biomedical Engineering, School of Science and Engineering, Duquesne University, Pittsburgh, PA, USA

ARTICLE INFO

Keywords:
Abdominal aortic aneurysm (AAA)
Patient-specific computational models
Intraluminal thrombus (ILT)
Oxygen transport
Vasa vasorum (VV)
Computational fluid dynamics (CFD)

ABSTRACT

The mechanisms of abdominal aortic aneurysm (AAA) formation and rupture are controversial in the literature. While the intraluminal thrombus (ILT) plays a crucial role in reducing oxygen flux to the tissue and therefore decreasing the aortic wall strength, other physiological parameters such as the vasa vasorum (*VV*) oxygen flow and its consumption contribute to altered oxygenation responses of the arterial tissue as well. The goal of this research is to analyse the importance of the aforementioned parameters on oxygen delivery to the aneurysmal wall in a patient-specific AAA. Numerical simulations of coupled blood flow and mass transport with varying levels of *VV* concentration and oxygen reaction rate coefficient are performed. The hypoperfusion of the adventitial *VV* and high oxygen consumption are observed to have critical effects on reducing aneurysmal tissue oxygen supply and can therefore exacerbate localized oxygen deprivation.

1. Overview and background

An abdominal aortic aneurysm (AAA) is an enlargement of the infrarenal aorta that develops asymptomatically over long periods of time as a result of arterial wall remodeling and degradation of the extracellular matrix [1] and can be life-threatening if ruptures [2]. Acute AAA rupture has a mortality rate of over 80% [3] with deaths related to AAA classified as the 14th main cause of mortality in the United States [4,5]. In addition, it has been approximated that AAA ruptures cause about 5% of sudden deaths in developed countries [6]. Despite these critical statistics, the mechanisms behind AAA progression remain unclear.

AAA is found to be associated with the formation of a layer called an intraluminal thrombus (ILT) which exists in over 75% of aneurysm cases [7]. Indeed, in almost 80% of the patients studied clinically, AAAs ruptured in the areas where ILT was present [8]. The regions of the aneurysmal wall tissue beneath a large ILT experience localized oxygen deprivation (i.e., hypoxia). This reduction of oxygen supply and the resulting hypoxic environment in AAA causes inflammation [9] and structural degradation of the arterial tissue [10]. Hence the oxygen loss leads to decreased mechanical strength of the wall [11], increasing the chance of AAA development and fatal rupture [12].

The “hypoxia-mediated wall weakening” theory have been explored in a few previous research and it has been hypothesized that sufficient transluminal oxygen transport is a crucial factor to nourish the arterial wall and stimulate the collagen and elastin production in the tissue, which can support its structural integrity and strength [13,14]. A comprehensive summary of these aforementioned investigations on the potential importance of hypoxia is provided in [15]. Additionally, in prior studies on the importance of hypoxia in vascular mechanics and its potential link to aneurysm progression, the significance of various oxygen transport parameters in AAA context are quantified [14,16,17]. In particular, using a fluid-structure interaction (FSI) methodology, the impact of the ILT presence on oxygen flow in patient-specific aneurysm models is identified in [18], while the relationship between ILT and aneurysm geometrical variations with localized oxygen starvation in idealized AAA models is demonstrated in [19]. A similar study was performed in [20] on a patient-specific AAA geometry to observe the effects of ILT porosity and its permeability on oxygen delivery. Moreover, the effects of oxygen transport properties were shown in idealized geometries with varying ILT stratification, i.e., single-layer or multi-layer ILT domains in [21]. In some former models, the effect of hemodynamic features on mass transport had been neglected (i.e., [14,22,23]). However, the blood flow is proven to affect the arterial wall mass transfer, in particular in the regions with disturbed flow patterns [24].

While tissue hypoxia has been observed as an indication of AAA rupture [13] and the effects of ILT morphology [14,19] and structural

* Corresponding author.
E-mail address: zakerzadehr@duq.edu (R. Zakerzadeh).

https://doi.org/10.1016/j.csbj.2023.10.008
Received 1 August 2023; Received in revised form 5 October 2023; Accepted 6 October 2023
Available online 8 October 2023
2001-0370/© 2023 The Author(s). Published by Elsevier B.V. on behalf of Research Network of Computational and Structural Biotechnology. This is an open access article under the CC BY-NC-ND license (http://creativecommons.org/licenses/by-nc-nd/4.0/).

composition [21,25] on arterial wall hypoxia in AAA have been extensively studied and validated, another factor that contributes to the oxygenation of the AAA tissue is the adventitial vasa vasorum (*VV*) blood supply, which plays a key biochemical role in aortic wall nourishment and therefore the corresponding tissue mechanics and AAA progression. The arterial *VV* is a microvascular network, which helps the parent vessel by delivering oxygen and other essential nutrients (Fig. 1a). The arterial *VV* exists in arteries with a thicker wall (higher than 0.5 mm wall thickness) and their density varies by anatomic location within the aorta [26]. In fact, the *VV* network have the largest density in the aortic arch, decreases distally and in the infrarenal abdominal aorta reaches the lowest value. Moreover, although *VV* is limited in the exterior portion of the human abdominal aorta and does not penetrate the medial layer [27], histopathological studies have been reported the presence of medial microvasculature and increased microvascular density for AAAs [28,29].

Previous histological analysis of the human arterial wall tissues identified occlusion and stenosis of the *VV* during open repair of the infrarenal AAAs [30]. This observation suggests that *VV* blood flow and oxygenation to the vessel wall can be reduced, leaving the aorta particularly susceptible to hypoxia [31]. At the same time, the oxygen requirements would be altered for the diseased aorta. On this basis, it has been suggested that the balance between the supply and demand of oxygen in the aneurysmal wall may be important for the fate of the initiated lesion and its progress.

Further support for the theory that hypoperfusion of *VV* invokes and exacerbates progression of AAA comes from work in animal models [32–34]. These studies demonstrate that when *VV* perfusion is physically compromised, wall hypoxia and degeneration occur, which results in histological phenomena reminiscent of human aneurysmal pathology. However, since certain physiological parameters such as *VV* oxygen flow and its consumption rate are not directly measurable, computational models would be helpful to investigate the importance of this effect and assess the contribution of *VV* to provide oxygen supply within the aortic tissue. In most of the prior mentioned computational models that simulated the risk of aneurysmal tissue oxygen deprivation, the presence of *VV* had been neglected, despite the likely key role that this source of nutrients plays in oxygen delivery within the AAA. Although the sensitivity of some oxygen distribution metrics to the *VV* was previously analyzed for a simplified AAA geometry [17], the combined contribution of *VV* oxygen flow to arterial wall oxygenation and the effects of tissue oxygen consumption in anatomically realistic AAA models have not been explored in any of the prior studies.

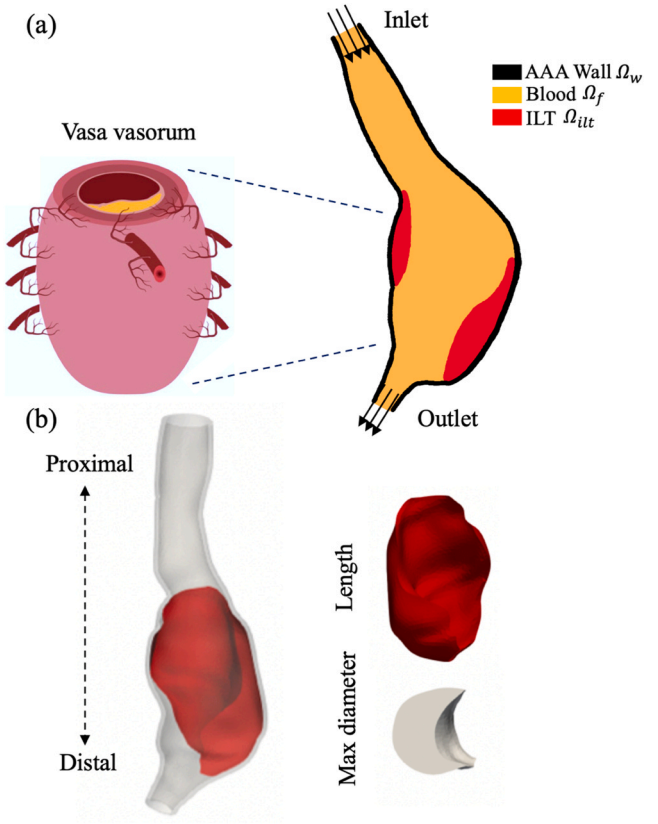

Fig. 1. (a) Description of a patient-specific AAA geometry with ILT region and *VV* vessels in the infrarenal abdominal aorta, taken from [29] (CC BY-NC). (b) The considered computational model including the same three domains: aortic wall displayed in grey, ILT in red, and the lumen. The ILT length, and ILT maximum diameter defined at a cross section at the height where ILT thickness is the largest, are identified.

Given the limited research on assessing the significance of *VV* supply on tissue nourishment and its link to AAA hypoxia, our aim in this paper is to develop a coupled computational framework to simulate the blood flow and oxygen transport in a patient-specific model of AAA that contains an ILT, and therefore, investigates the effects of the *VV* and oxygen reaction rate on oxygen delivery to the aneurysm tissue. More precisely, in an ILT-bearing AAA, the extent to which *VV* oxygenation and the subsequent oxygen consumption influence the oxygenation of the arterial wall will be analyzed. Considering that the data related to *VV* oxygen flow and arterial tissue oxygen consumption are hard to obtain experimentally, a parametric study will be performed and the influence of these features as well as the sensitivity of the model outcomes to the chosen value of the aforementioned parameters will be explored. Particularly, numerical simulations with physiologically meaningful variations of oxygen concentration imposed on adventitia and reaction rate coefficient will be performed to quantify concentrations in the wall region and compare oxygen distributions contours among the simulated cases.

2. Problem formulation and modelling

The mathematical model used for the lumen, ILT, and arterial wall regions, as well as computational details and boundary conditions are provided in this section. Fig. 1a. illustrates the considered AAA model to perform coupled simulation of hemodynamics-mass transport, while Table 1 lists physical parameters and their related values for each domain. The variables and parameters for the lumen, aortic wall, and the ILT tissue are identified using *f*, *w*, and *ilt* subscripts, respectively. We have created the AAA model (Fig. 1b) from computed tomographic (CT) scans and segmented the lumen and ILT domains in the SimVascular software [35]. The vessel is extruded to form a 2 mm thickness. The obtained AAA patient-specific model computational domain has an aneurysm bulge with a length of 82.3 mm and a maximum diameter of 48.0 mm, while the ILT geometry is characterized with a maximum thickness and length of 17.4 mm and 81.6 mm, respectively.

Table 1
Summary of parameters and material properties.

Domain	Parameter description	Parameter value
Blood	Density ρ_f	1050 kg/m^3
	Dynamic viscosity μ_f	0.0035 kg/m.s
	Oxygen diffusion coefficient D_f	1.6×10^{-9} m^2/s [56]
	Inlet oxygen concentration C_f^{in}	5.12×10^{-3} kg/m^3 [14]
	Vasa vasorum oxygen concentration *VV*	2.56×10^{-3} kg/m^3 [49] for Baseline case See Table 2 for variations
Wall	Oxygen diffusion coefficient D_w	1.08×10^{-9} m^2/s [57]
	Reaction rate *r*	10^{-3} s^{-1} for Baseline case See Table 2 for variations
ILT	Oxygen diffusion coefficient D_{ilt}	1.34×10^{-9} m^2/s

2.1. Modelling hemodynamic and oxygen transport in the blood

The aortic blood flow model in the lumen is governed by the Navier-Stokes equations for an incompressible, viscous Newtonian fluid in a steady laminar flow, given by:

$$\rho_f(\boldsymbol{U}_f.\nabla\boldsymbol{U}_f) = \nabla.\boldsymbol{\sigma}_f \ in\ \Omega_f \tag{1}$$

$$\nabla.\boldsymbol{U}_f = 0\ in\ \Omega_f \tag{2}$$

The blood velocity and its density are represented by $\boldsymbol{U}_f$ and ρ_f, respectively, and the Cauchy stress tensor in the fluid domain is defined as $\boldsymbol{\sigma}_f = -p_f\boldsymbol{I} + 2\mu_f\boldsymbol{D}(\boldsymbol{U}_f)$ where $\boldsymbol{D}(\boldsymbol{U}_f) = \frac{1}{2}(\nabla\boldsymbol{U}_f + \nabla\boldsymbol{U}_f{}^T)$ is the symmetric part of the velocity gradient, p_f is the blood pressure, and μ_f is the blood dynamic viscosity.

The non-Newtonian viscosity of blood has been found to have a minor importance in the dynamics of blood flow [36,37] and mass transport [38] in the large arteries of interest, particularly for the average range of shear rates reported in the aorta [39]. In addition, the flow is assumed to be steady based on the high Schmidt number characterizing the phenomenon [40], which provides a reasonable approximation to time-averaged unsteady results. Details on the justification of this assumption are provided in the Conclusions section.

The blood flow in the lumen is coupled with oxygen transport, which is governed by the convection-diffusion equation. In Eq. (3), C_f denotes the oxygen concentration in the lumen, while the oxygen diffusion coefficient in the blood flow is defined by D_f. We note that the objective of this model is to compare the relative oxygen transport over the thrombus and aneurysmal wall; therefore, the effects of oxygen binding to hemoglobin on concentrations is not considered.

$$\nabla \bullet \left(-D_f\nabla C_f + \boldsymbol{U}_f C_f\right) = 0\ in\ \Omega_f \tag{3}$$

2.2. Modelling oxygen transport in the AAA wall and ILT tissue

The diffusion-reaction equation with uniform oxygen consumption is adopted for oxygen transport in the aortic wall:

$$\nabla \bullet (-D_w\nabla C_w) = rC_w \quad in \quad \Omega_w \tag{4}$$

In Eq. (4), C_w and D_w represent the oxygen concentration and oxygen diffusion coefficient in the wall region, respectively. Also, rC_w denotes the reaction term for modelling the oxygen metabolic consumption by the smooth muscle cells, with the constant parameter r for the oxygen reaction rate [41]. The oxygen transfer in the ILT is governed by the diffusion equation without any smooth muscle cells to consume oxygen, represented by:

$$\nabla \bullet (-D_{ilt}\nabla C_{ilt}) = 0 \quad in \quad \Omega_{ilt} \tag{5}$$

In Eq. (5), C_{ilt} and D_{ilt} represent the oxygen concentration and oxygen diffusion coefficient in the ILT region, respectively. It should be noted that for oxygen transfer in the wall tissue and the ILT, the contribution of connective transport is neglected, and these domains are considered to be impermeable to interstitial fluid flow (i.e., the movement of the fluid through the extracellular matrix in the tissue). We have extensively justified the impermeable ILT assumption in previous research [17]. Additionally, by including the permeable feature of the ILT and wall tissues and comparing oxygen delivery metrics for a range of permeability values, we observed that model predictions did not change significantly with a poroelastic model [20].

2.3. Simulation setup and coupling aspects

Physiological boundary conditions are prescribed at the proximal and distal cross-sectional areas of the lumen, respectively (see Fig. 1b for anatomical orientations). At the inlet, a uniform pressure of $p_f^{in} = 130$ mmHg is considered [42], while a mass flow rate of 0.075 kg/s is applied at the outlet, in agreement with the experimental measurements of the abdominal aorta [43] and the average volumetric blood flow data acquired at the infrarenal aorta in AAA patients [44]. The Reynolds number is calculated based on the entrance lumen diameter and the inflow boundary condition, and its value of 1600 is within the physiological range recorded in the abdominal aorta [45].

To define the appropriate boundary conditions for the oxygen transport, the concentration at the lumen inlet is defined as 5.12×10^{-3} kg/m^3. This value is obtained by assuming the oxygen tension as 100 mmHg, which corresponds to the average saturation of 97.7% in human blood flow. To model the *VV* flow, a partial pressure of oxygen is applied on the exterior surface of the aortic wall. Furthermore, for the oxygen flow, a zero-flux condition at the two ends of the cross-sectional areas of the wall (inlet and outlet) is considered, while a continuity condition and conservative interface flux conditions at the boundaries between the lumen, ILT, and wall regions are prescribed. The interfaces are identified as Γ_{ilt-w} between the ILT and the wall, Γ_{f-w} between the lumen and the wall, and Γ_{f-ilt} between the ILT and the lumen. Accordingly, the continuity and flux interface conditions are described by Eq. (6), where $\boldsymbol{n}$ is the surface normal direction.

$$C_f = C_w,\ \left(\boldsymbol{U}_f C_f - D_f\nabla C_f\right).\boldsymbol{n} = (-D_w \bullet \nabla C_w).\boldsymbol{n} \quad on \quad \Gamma_{f-w}$$

$$C_f = C_{ilt},\ \left(\boldsymbol{U}_f C_f - D_f\nabla C_f\right).\boldsymbol{n} = (-D_{ilt} \bullet \nabla C_{ilt}).\boldsymbol{n} \quad on \quad \Gamma_{f-ilt}$$

$$C_{ilt} = C_w,\ (-D_{ilt} \bullet \nabla C_{ilt}).\boldsymbol{n} = (-D_w \bullet \nabla C_w).\boldsymbol{n} \quad on \quad \Gamma_{ilt-w} \tag{6}$$

The commercial platform ANSYS CFX Workbench Software (v.22.2, ANSYS Inc., Canonsburg, PA, USA) is used to conduct the coupled simulations of blood flow and oxygen transport in AAA domains. The mass transfer (Eqs. (3) – (5)) is incorporated in the CFX-solver by using the transport equations and inserting an additional variable (non-reacting scalar) for oxygen. ANSYS CFX-Solver Theory Guide provides further information on several types of governing equations supported by the solver for the additional variable [46]. Namely, the transport equation is solved for this additional variable in blood flow to represent convective and diffusive oxygen delivery in the lumen (Eq. (3)), while the diffusive transport equations which exclude the advection term are adopted for the ILT and arterial wall. Additionally, the non-zero source term in Eq. (4) is implemented as a user-defined function to account for oxygen consumption in the wall region. The interfacial flux and appropriate boundary values are also prescribed for the additional variable.

Eqs. (1) – (6) are implemented and numerically evaluated via a monolithic approach, and the system is solved using an algebraic multigrid method exploiting incomplete LU factorization as smoother. The advection terms in momentum equations are discretized by a second-order upwind interpolation scheme, while the second-order centered differencing scheme evaluates the diffusive terms in the momentum equation and oxygen transport equation of the blood flow. The variables for the blood pressure and velocity in the Navier-Stokes equations are approximated at the identical node. Additionally, the Picard iterations is adopted to linearize convective term of the Navier-Stokes equations. Also, considering that turbulence features did not appear in the flow of the simulated AAA, and the obtained value of the Reynolds number ($Re_{max} = 1600$), the *DNS* method for laminar flow is employed for the solution. Finally, the convergence criteria of 10^{-6} based on the residuals for the mass and momentum equations is chosen.

The open-source software Gmsh [47] is adopted to discretize the three computational domains, namely, blood, ILT and the aneurysmal wall; using linear tetrahedral elements. To ensure an optimally sized discretization, mesh convergence analysis is carried out in the same manner to the previous research in [18]. Particularly, the sensitivity test is accomplished by increasing the number of elements and conducting the simulations with refined grid density until the re-calculated model predictions agreed well with that from the original mesh. The solution

for blood velocity and pressure, as well as the oxygen concentration at some examined sections were recorded, and the resolution was considered sufficient for a relative error lower than 5% in terms of these simulation outcomes. It has been also observed that the maximum difference in wall oxygen concentration between coarser and finer meshes was less than 3.8%, hence, the grid-independent results were obtained using 188,219 linear tetrahedral elements in the fluid domain and 132, 281 and 80,250 linear tetrahedral elements in the AAA and ILT domains, respectively. The mesh resolutions of the patient-specific case were also identical to those reported in the computations of [48].

2.4. Parametric study

Influence of the *VV* and reaction rate, *r*, on oxygen flow is investigated by performing a parametric study with different levels of oxygen concentration on the arterial wall external boundary and varying values for the reaction rate constant, all simulated with the same patient-specific geometry previously described. Eight models are constructed from Case 1 to Case 8 and summarized in Table 2. Case 4 represents the baseline model with values that are considered physiological for the adventitial oxygen concentration and the reaction rate constant. Particularly, the oxygen partial pressure on the adventitia surface is approximated to be around half of its value in the blood flow according to previous experimental studies [49–51]. Therefore, the physiological value for the *VV* oxygen concentration of the baseline case is assumed to be 2.56×10^{-3} kg/m^3 on the exterior wall surface which is consistent with 50 mmHg for the oxygen partial pressure.

Four sets of *VV* oxygen supply are considered, ranging from neglecting the presence of the *VV* to its physiologically normal value, with a doubled increase in respective cases. Specifically, Cases 1 – 4 are modeled with the oxygen concentration on the exterior wall surface of $VV_1 = 0$ kg/m^3, $VV_2 = 0.64 \times 10^{-3}$ kg/m^3, $VV_3 = 1.28 \times 10^{-3}$ kg/m^3, and $VV_4 = 2.56 \times 10^{-3}$ kg/m^3. These cases are simulated while the reaction rate coefficient is kept constant at the value of $r = 10^{-3}$ s^{-1}.

Furthermore, to measure the influence of the oxygen consumption term on concentrations within the AAA, the reaction rate coefficient is varied with exponentially increasing values of $r = 10^{-4}$, 10^{-3}, 10^{-2}, 10^{-1}, and 1 s^{-1} while *VV* is kept constant at the previous specified value of 2.56×10^{-3} kg/m^3 for the baseline case. Using different reaction rates mentioned above, Cases 5 – 8 are considered. The baseline model for comparison (Case 4) has a reaction rate of 10^{-3} s^{-1}. The parameter sets for all simulated cases are demonstrated in Table 2. After carrying out the coupled simulations for each case, the flow and concentration outcomes are obtained and discussed in the next section.

3. Results and discussion

For the baseline simulation (Case 4), a prediction of blood flow pattern inside the AAA lumen using the velocity streamlines is provided in Fig. 2, showing complex fluid trajectories and recirculation vortex in the AAA bulge region. The flow is sluggish in the aneurysm sac and the velocity increases at the outlet due to the smaller diameter of the vessel. We note that the formation of helical flow patterns in Fig. 2 happens because of the steady flow and the uniform pressure boundary condition enforced at the inlet of the fluid domain, while under the pulsatile flow, the spatial variation of blood velocity in the aneurysm at individual phases will change and the recirculation zone may not exist throughout the cardiac cycle. Moreover, the blood velocity within the aneurysm (Fig. 2) is comparable with the average value of ≈ 0.2 m/s detected in AAA [52,53], and the corresponding Reynolds number is observed to be within the range of physiological Reynolds numbers recorded in the abdominal aorta [45]. Results also demonstrate a physiologically realistic pressure distribution (contour is not shown) in the lumen; the pressure value at the proximal surface is around 1.74×10^4 Pa ≈130 mmHg, and a small pressure drop of ~200 Pa is observed between the two endings of the aorta.

Table 2
Parameter sets for simulated cases.

	Vasa vasorum oxygen concentration (kg/m^3)	Reaction rate (s^{-1})
Case 1	$VV = 0$	$r = 10^{-3}$
Case 2	$VV = 0.64 \times 10^{-3}$	$r = 10^{-3}$
Case 3	$VV = 1.28 \times 10^{-3}$	$r = 10^{-3}$
Case 4 - Baseline	$VV = 2.56 \times 10^{-3}$	$r = 10^{-3}$
Case 5	$VV = 2.56 \times 10^{-3}$	$r = 10^{-4}$
Case 6	$VV = 2.56 \times 10^{-3}$	$r = 10^{-2}$
Case 7	$VV = 2.56 \times 10^{-3}$	$r = 10^{-1}$
Case 8	$VV = 2.56 \times 10^{-3}$	$r = 1$

Fig. 3a shows the oxygen distribution of Case 4 (baseline) in three cross-sections along the ILT region of the aneurysm. These surfaces are positioned at the top of the aneurysm neck (T), center of the enlarged region (C), and the base of the bulge (B), with the concentration contour at the center profile magnified. The magnified cross-sectional contour indicates the highest concentration in the lumen, with a gradually decreasing rate inside the tissue and the minimum value on the wall abluminal surface at the edge of the cross-section (Fig. 3a). Additionally, the aortic wall concentration decreases significantly at the portion that is in contact with the ILT. By comparing the simulated results for the baseline case with the previous in situ and in vitro measurements of wall oxygenation, we have previously validated the oxygen transport model in [18]. Specifically, comparisons are made with measurements of oxygen tension in surgically removed AAA wall specimens [13] and the partial pressures of oxygen in a dog's abdominal aorta [50]. A qualitative agreement with these experimental results is noticed.

In addition, the results of the numerical simulations of the eight cases introduced in the Parametric study section with various levels of oxygen concentration on the *VV* surface and reaction rate constants are presented. Particularly, several measures for oxygen concentration within the AAA tissue and ILT are computed and analysed to explore the significance of these parameters. The contours of oxygen concentration distributions within the ILT region of AAA are demonstrated in Fig. 3b-c for each case, on three profiles; T, B, and C, mentioned above. The cross-sections for each of these plots are placed at the same position for the eight cases.

For all the cases (Fig. 3b-c), the highest concentration is observed at the portion of the thrombus where it contacts the blood region, which is close to the concentration inside the lumen and is shown by an orange-yellow color. The cross-sections of Fig. 3b represent cases with varying *VV* values to demonstrate the comparison of the oxygen distribution in the ILT obtained by varying the adventitial concentration based on the protocol in Table 2. Namely, Case 1, Case 2, Case 3, and Case 4 have adventitial oxygen concentration of 0, 0.64×10^{-3}, 1.28×10^{-3}, and 2.56×10^{-3} kg/m^3, respectively (Fig. 3b). The reaction rate value is kept consistent between Cases 1– 4 at 10^{-3} s^{-1}. Conversely, the cross-sections profiles of Fig. 3c represent simulated cases where the reaction rate constant *r* is varied.

Cross-sectional contours of Fig. 3b show a significant decrease in concentration along the interior of the arterial wall in cases with lower *VV* oxygen pressure; while with increasing *VV* values, a significant increase in oxygen concentration along the lateral part of the ILT which is in contact with inner wall is observed. Among Cases 1, 2, 3 and 4, Case 1 has the lowest concentration of oxygen at the edge of the ILT domain while Case 4 has the highest concentration in that region. Thus, as the *VV* value increases from VV_1 to VV_4, the flow of oxygen to the arterial wall also increases.

Moreover, in Fig. 3c, reaction rate constants of $r = 10^{-4}$, 10^{-2}, 10^{-1}, and 1 s^{-1} are considered for Case 5, Case 6, Case 7, and Case 8, respectively. These cases are simulated with the same *VV* as the baseline model. The differences in the ILT oxygen concentrations are not as drastic in the cases within increasing reaction rate (Fig. 3c) compared to the cases with increasing *VV* values (Fig. 3b). Specifically, no noticeable

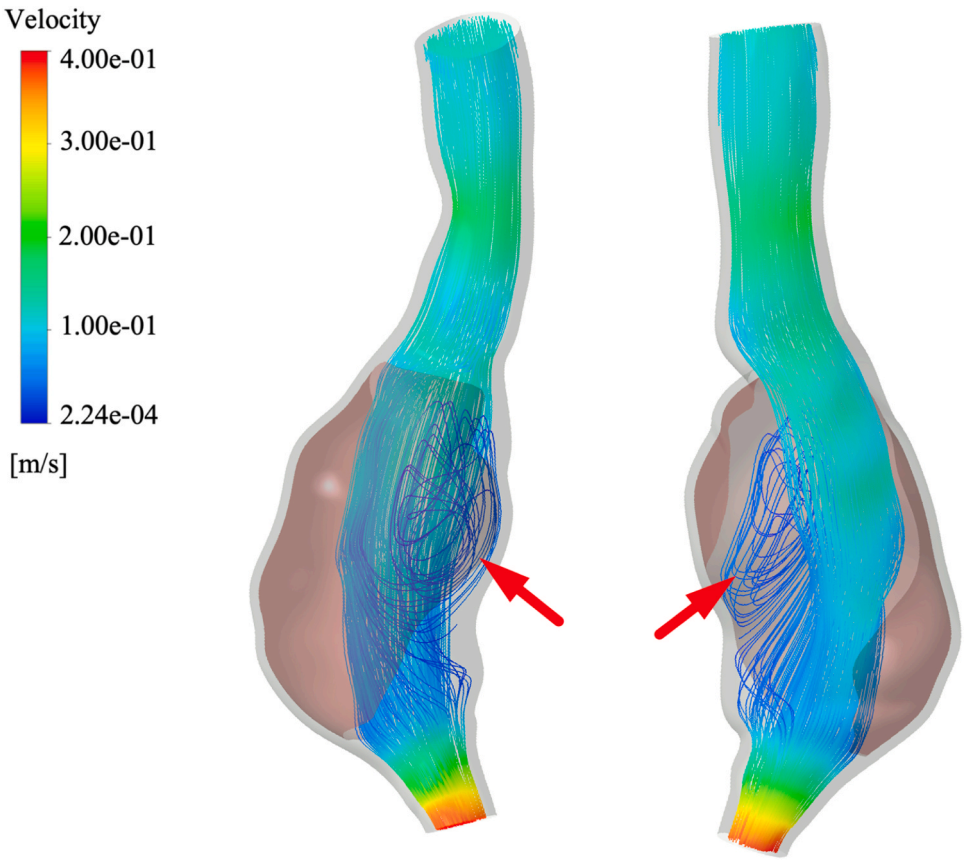

Fig. 2. Velocity streamlines displayed for steady flow in the investigated anatomically realistic AAA model, with recirculation flow patterns inside the bulge region (red arrows).

difference is observed between oxygen distribution profiles of Cases 6, 7, and 8 which vary by a 10-fold increase of reaction rate between subsequent cases. However, by decreasing the reaction rate from 10^{-3} s^{-1} in the baseline model to 10^{-4} s^{-1} in Case 5 (the first contour of Fig. 3c), a pronounced increase in the oxygen distribution is noted. Similarly, the contours in Case 6, which is modeled with a reaction rate of $r = 10^{-2}$ s^{-1}, demonstrate a distinct decrease in concentrations on the lateral boundary when compared to the baseline model ($r = 10^{-3}$ s^{-1}). As the arterial wall oxygen consumption increases, the concentrations along the exterior of ILT region decrease, as expected.

The oxygen concentrations for all the simulated cases are plotted along the arterial wall surface at the portion that the wall tissue is in contact with the ILT and are compared in Fig. 4. The red line represents the baseline case information with the physiological *VV* and reaction rate, while the blue and black lines represent the concentration values for cases with varying *VV* oxygen supplies and differing reaction rate, respectively. The cases are outlined in Table 2. The bottom panel of Fig. 4 shows a zoomed portion of the plot since a significant difference between the data sets for the cases with higher reaction rates could not be observed. As demonstrated previously in Fig. 3, results in Fig. 4 confirm that an increase in the adventitial oxygen concentration results in a higher values of oxygen at the interface between the ILT and arterial wall. Moreover, a drastic increase is shown between the baseline case and Case 5 when the reaction rate is decreased from 10^{-3} s^{-1} to 10^{-4} s^{-1}. A large decrease is demonstrated when the reaction rate is increased from 10^{-3} to 10^{-2} s^{-1} in Cases 4 and 6, respectively. However, when increasing the reaction rate by the power of 10 among Cases 6, 7, 8, the differences in oxygen concentration along the inner wall of the tissue are minimal between the simulations.

Furthermore, the volumetric average of oxygen concentration in the AAA wall region $\overline{C_w}$ and the corresponding percent change $\delta_{\overline{C_w}}$ are obtained by Eq. (7) and summarized in Table 3. The $\delta_{\overline{C_w}}$ for each case is obtained using the measured average concentrations of the case and the baseline values of Case 4. Fig. 5 illustrates the comparison of the results for various cases.

$$\overline{C_w} = \frac{\int_{\Omega_w} C_w \quad d\Omega_w}{\int_{\Omega_w} d\Omega_w}$$

$$\delta_{\overline{C_w}} = \left| \frac{\overline{C_w}_{\ baseline} - \overline{C_w}}{\overline{C_w}_{\ baseline}} \right| \times 100\% \tag{7}$$

The data in Fig. 5 illustrate an increase in volumetric oxygen concentration, $\overline{C_w}$, within the arterial wall as the adventitial oxygen increases. The AAA wall domain in Case 1 that neglects the supply of oxygen by the *VV* has an average oxygen concentration of 4.357×10^{-4} kg/m^3. Each subsequent case doubles in *VV* value up to Case 4 with the baseline *VV* value, and the volumetric oxygen concentration of the aortic wall increases by approximately 2×10^{-4} kg/m^3 between each case. Specifically, Cases 2, 3, and 4 have average oxygen concentrations of 6.429×10^{-4}, 8.143×10^{-4}, and 1.159×10^{-3} kg/m^3, respectively. Therefore, the percent differences of $\delta_{\overline{C_w}}$ between the baseline concentration and the concentrations decrease consistently for each case with increasing *VV* value. The specific values for these percentages are compiled in Table 3.

As demonstrated in Table 3 and Fig. 5, the greatest volumetric oxygen concentration, $\overline{C_w}$, is captured in Case 5 which has the physiological *VV* value of the baseline case and the minimum value of reaction rate $r = 10^{-4}$ s^{-1}, and it causes the wall concentration to increase 124.22% from the baseline value. For Case 6, Case 7, and Case 8, which are characterized by gradual increases in the reaction rate, the

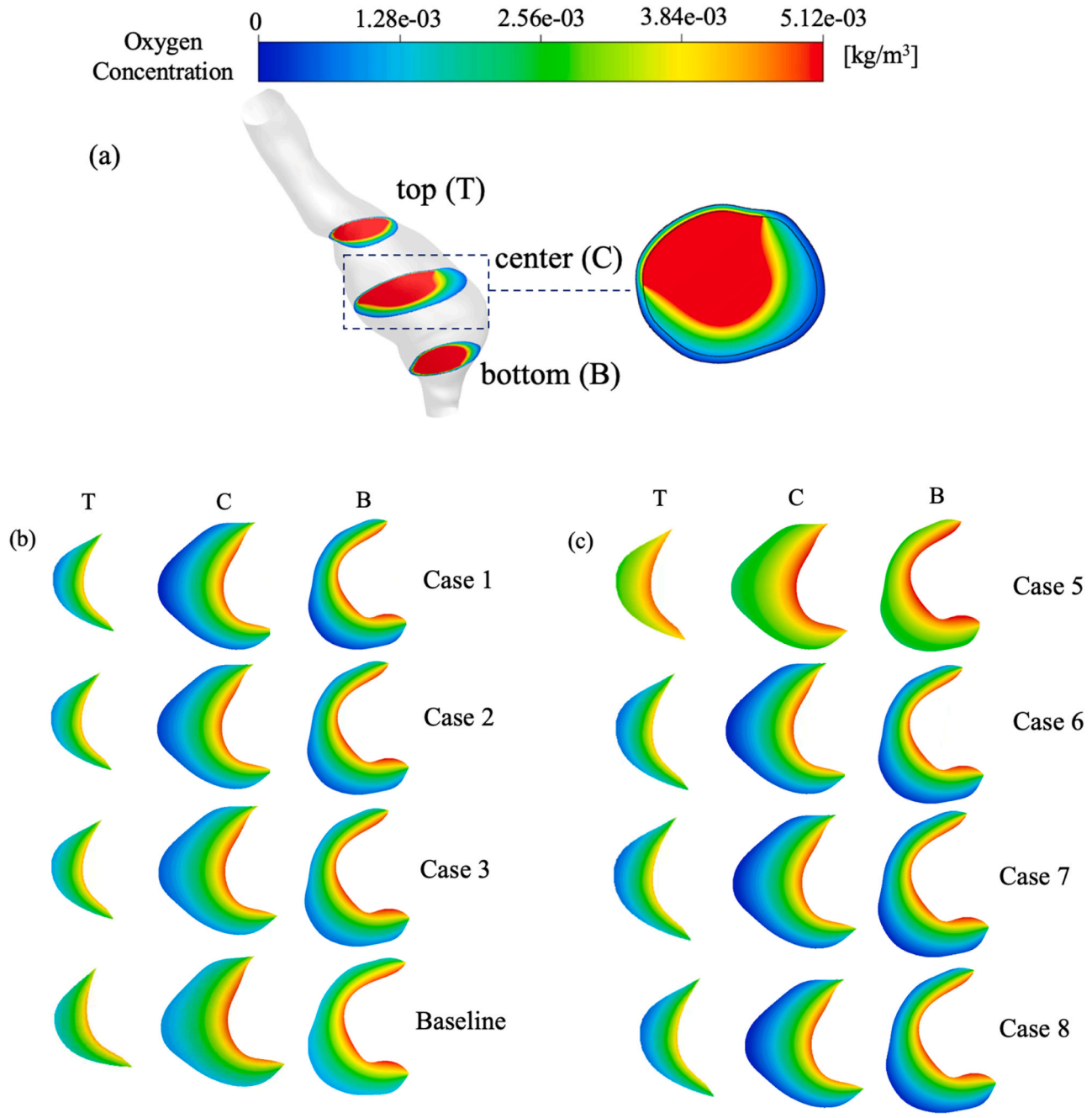

Fig. 3. (a) Demonstration of cross-sectional areas with a magnified concentration contour at the central profile of baseline case. Panel (b) represents cases with variations in *VV* value while panel (c) represents cases with different reaction rates.

volumetric oxygen concentration decreases 84.97%, 98.44%, and 99.84%, respectively, from the arterial wall oxygen supply of the baseline case. While $\overline{C_w}$ for these cases is significantly smaller than the average volumetric oxygen concentration of the baseline case, the difference between them is minimal.

The results of Figs. 3–5 demonstrated that a lack of oxygen nourishment from the *VV* induced hypoxic conditions. Specifically, with the absence of the *VV* (Case 1) or high reaction rate values (Cases 6–8), it has been observed that the concentrations are significantly reduced and the oxygen supply is depleted at the arterial wall inner surface (Figs. 3–4). Moreover, results for the volumetric average of aortic wall oxygen, $\overline{C_w}$, display detectable variations to the adventitial concentration (Fig. 5). It is observed that the $\overline{C_w}$ variations are also pronounced to changes in the reaction rate. Namely, an excessive increase in oxygen demand attenuates concentrations in the aortic tissue and causes oxygen deprivation.

4. Conclusions

In an innovative approach relative to the work done in the field, the oxygenation of the AAA arterial wall by considering variable *VV* concentration and oxygen consumption is numerically investigated in this manuscript. While the ILT prominently contributes to oxygen flux reduction, consequently impacting aortic wall integrity, other physiological effects such as *VV* oxygen flow intricately participate in modulating arterial tissue oxygenation. In fact, clinical results confirm that hypoperfusion of *VV* (i.e., the reduced or blocked *VV* flow) causes medial hypoxia and has a critical effect on AAA development [32–34].

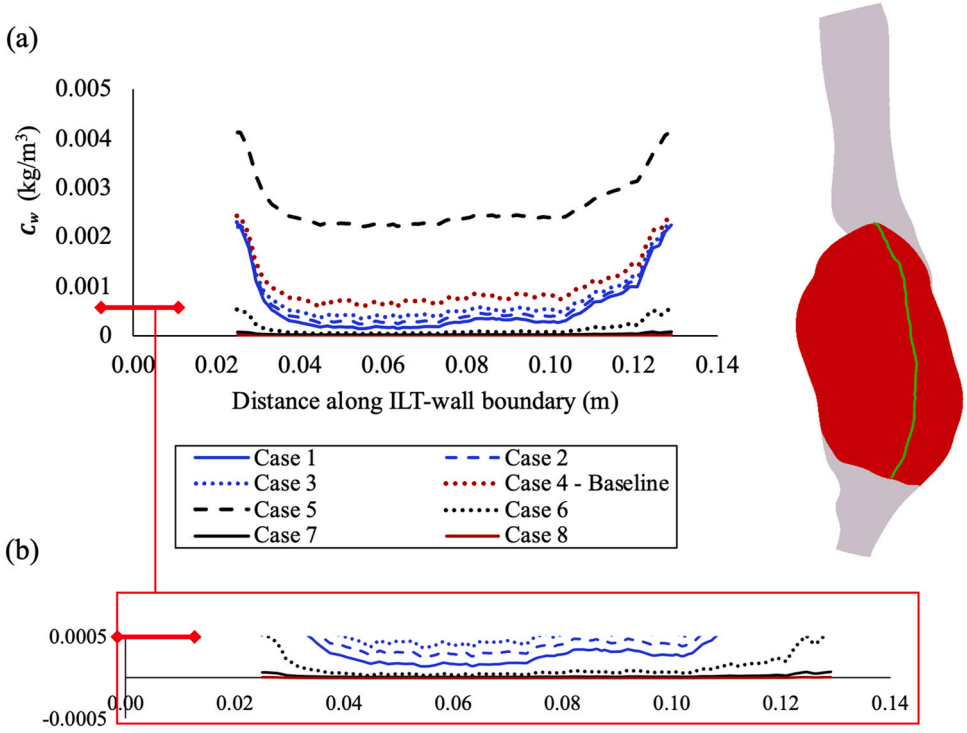

Fig. 4. Concentrations in the wall region at the ILT covered portion of the model (path line is shown by green on the schematic representation) for varying *VV* oxygen supply (Cases 1 – 4) and reaction rate constant (Cases 5 – 8). The cases are presented in Table 2. (b) A zoomed part of the plot for the hypoxic range (low levels of oxygen) $C_w \leq 5 \times 10^{-4} \frac{\text{kg}}{\text{m}^3} \approx 10$ mmHg. Overlapping values in Case 7 and Case 8 with high oxygen reaction rates are observed.

Table 3
Average wall oxygen concentrations $\overline{C_w}$ and their percentage difference $\delta_{\overline{C_w}}$ in reference to the baseline are obtained (Eq. (7)). Case 5 shows an increase in oxygen compared to the baseline while others have a decrease.

Case ID	$\overline{C_w}$ (kg/m^3) $\times 10^{-4}$	$\delta_{\overline{C_w}}$(%)
Case 1	4.357	63.46 ↓
Case 2	6.249	47.60 ↓
Case 3	8.143	31.72 ↓
Case 4 - Baseline	11.95	0
Case 5	26.73	124.22 ↑
Case 6	0.946	84.97 ↓
Case 7	0.1858	98.44 ↓
Case 8	0.0186	99.84 ↓

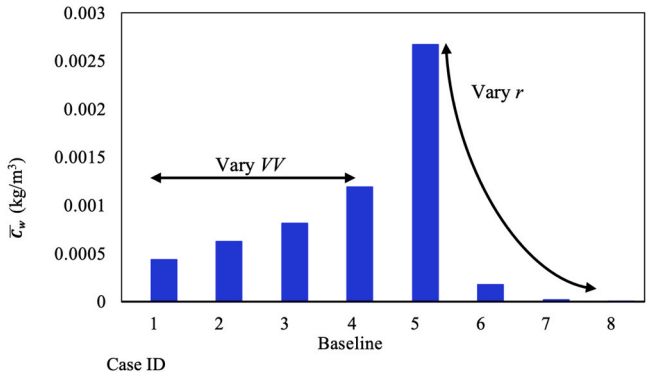

Fig. 5. Average concentrations in the wall region ($\overline{C_w}$) from Table 3 data.

In addition, the metabolic consumption of oxygen varies within the arterial wall [50]. However, the influence of these parameters on oxygen transport is neglected in many previous AAA models. The potential clinical impact of the presented computational framework is in its contribution to highlight the importance of oxygen supplied by *VV* and investigate how changes in *VV* flow conditions affect oxygen delivery to the aneurysmal wall in a patient-specific AAA context, which is not measurable non-invasively. The results from this study will help to guide the future computer simulations of AAA by providing essential information on the significance of various oxygen transport parameters. This can eventually advance the development of methods to explore the biomechanics of AAA tissue by in situ simulation and assess the potential risk of hypoxia and therefore complication risk of aneurysm cases in future research. The conclusions also help to refine diagnostic and treatment strategies for AAA, particularly those involving oxygen delivery to the arterial wall.

Coupled hemodynamics and oxygen transport simulations are performed with variations in the adventitial oxygen concentration and the reaction rate related to the oxygen consumption. Considering the physiological range of oxygen supply by *VV* in the baseline case improved oxygen transport in the AAA. The results demonstrated that the oxygen concentration within the AAA wall increased among the cases as adventitial oxygen concentration increased and as the reaction rate constant decreased. Directly in line with expectation based on the chosen boundary conditions, it has been observed that a higher *VV* oxygen concentration value on the exterior wall surface is correlated with higher transport rate to the tissue and causes a greater amount of oxygen to reach the arterial wall. However, disrupted *VV* blood flow led to a significant decrease in concentrations and prevents oxygen flow from reaching inner layers of the tissue. Similarly, with an increase in reaction rate, more oxygen is being extracted by the AAA wall, while the oxygen delivery by the blood is constant. Therefore, more oxygen is consumed and less reaches the aortic tissue. The investigation reveals that compromised adventitial *VV* perfusion and enhanced oxygen consumption notably diminish tissue oxygen availability, potentially exacerbating hypoxia. The observations of this study also indicate that the adventitial *VV* is required for oxygenation of the medial layer and this source of oxygen supply needs to be considered in AAA simulations. It is

important to note that the adventitial oxygen concentration in the baseline case represents a partial pressure of 50 mmHg which corresponds to a healthy infrarenal aorta [51] and has been used in previous AAA computational models [49], however, this value can be lower in the case of an aneurysm [30]. Nonetheless, involvement of arterial *VV* in computational modeling of AAA provides a chance to obtain realistic and physiological measures of oxygen within the tissue.

Some limitations of this study need to be considered in interpretation of the results. The simulations are performed for the steady-state blood flow conditions in the lumen. It has been observed that this assumption reasonably estimates time-averaged unsteady mass transfer for phenomenon with a high Schmidt number, i.e., in the order of thousands [40]. The calculated Schmidt number in our model is about 2100 by assuming the diffusion coefficient of 1.6×10^{-9} m^2/s for oxygen in blood flow, hence, the steady-state solution appears to be a suitable approach to calculate the oxygen flux and concentration patterns within the AAA. Nevertheless, this assumption also remarkably decreases the computing time and required resources for a fully coupled three-dimensional pulsatile fluid flow and mass transport problem. Effects of pulsation of blood flow on oxygen transport in aorta are investigated by several previous studies as well [38,54], and it was observed that the pulsatile flow conditions did not alter the percentage difference between oxygen concentration patterns on the luminal surface when compared to its corresponding steady flow simulation. Additionally, it should be noted that because of limitations in imaging and reconstruction techniques, a uniform thickness for the AAA wall throughout the entire aneurysm is modelled. Moreover, the arterial wall and ILT tissues are assumed to have a uniform structural composition for the purpose of modelling, while oxygen diffusion coefficient fluctuates in multiple tissue layers. Exploring the significance of these simplifying assumptions will be considered as one of the next directions of this study. However, including these levels of complexity in our simulations would not change the current conclusions of this work as they are applied for simulating all the cases and comparing the relative values. Considering that both laminar and turbulent flow patterns may be observed through the models of AAA [55], the effects of flow instabilities and turbulence on arterial mass transfer for various ranges of Reynolds number and lesion severity will be explored in future work. A larger sample population could also take into account a wider range of AAA geometries to reach a stronger conclusion. Finally, additional studies are needed to better delineate whether and how *VV* remodeling causes, exacerbates, or alleviates aneurysmal pathophysiology in the abdominal aorta and predict hypoxia induced inflammation response.

CRediT authorship contribution statement

Alexis Throop: Methodology, Data curation, Visualization, Writing – original draft. **Manoela Neves:** Visualization, Data curation, Writing – review & editing. **Rana Zakerzadeh:** Conceptualization, Supervision, Formal analysis, Validation, Writing – review & editing.

Declaration of Competing Interest

The authors declare that they have no known competing financial interests or personal relationships that could have appeared to influence the work reported in this paper.

Acknowledgments

Support for this research was provided by the Samuel and Emma Winters Foundation and the NSF award number CBET 2138225. We also thank Miguel Rodriguez and Shawn Shadden who provided the abdominal aneurysm model.

References

[1] Jana S, Hu M, Shen M, Kassiri Z. Extracellular matrix, regional heterogeneity of the aorta, and aortic aneurysm. Exp Mol Med 2019;51(12):1–15.
[2] Kühnl A, Erk A, Trenner M, Salvermoser M, Schmid V, Eckstein H-H. Incidence, treatment and mortality in patients with abdominal aortic aneurysms: an analysis of hospital discharge data from 2005–2014. Dtsch Ärzteblatt Int 2017;114(22–23):391.
[3] Kuivaniemi H, Ryer EJ, Elmore JR, Tromp G. Understanding the pathogenesis of abdominal aortic aneurysms. Expert Rev Cardiovasc Ther 2015;13(9):975–87.
[4] Oliver-Williams C, Sweeting M, Turton G, Parkin D, Cooper D, Rodd C, et al. Lessons learned about prevalence and growth rates of abdominal aortic aneurysms from a 25-year ultrasound population screening programme. J Br Surg 2018;105(1):68–74.
[5] Sakalihasan N, Michel J-B, Katsargyris A, Kuivaniemi H, Defraigne J-O, Nchimi A, et al. Abdominal aortic aneurysms. Nat Rev Dis Prim 2018;4(1):1–22.
[6] Aggarwal S, Qamar A, Sharma V, Sharma A. Abdominal aortic aneurysm: a comprehensive review. Exp Clin Cardiol 2011;16(1):11–5.
[7] Harter LP, Gross BH, Callen PW, Barth RA. Ultrasonic evaluation of abdominal aortic thrombus. J Ultrasound Med 1982;1(8):315–8.
[8] da Silva ES, Rodrigues AJ, de Tolosa EMC, Rodrigues CJ, do Prado GVB, Nakamoto JC. Morphology and diameter of infrarenal aortic aneurysms: a prospective autopsy study. Cardiovasc Surg 2000;8(7):526–32.
[9] Coutard M, Touat Z, Houard X, Leclercq A, Michel J-B. Thrombus versus wall biological activities in experimental aortic aneurysms. J Vasc Res 2010;47(4):355–66.
[10] Lim CS, Kiriakidis S, Sandison A, Paleolog EM, Davies AH. Hypoxia-inducible factor pathway and diseases of the vascular wall. J Vasc Surg 2013;58(1):219–30.
[11] Swedenborg J, Mäyränpää MI, Kovanen PT. Mast cells: important players in the orchestrated pathogenesis of abdominal aortic aneurysms. Arterioscler, Thromb, Vasc Biol 2011;31(4):734–40.
[12] Haller SJ, Crawford JD, Courchaine KM, Bohannan CJ, Landry GJ, Moneta GL, et al. Intraluminal thrombus is associated with early rupture of abdominal aortic aneurysm. J Vasc Surg 2018;67(4):1051–8. e1.
[13] Vorp DA, Lee PC, Wang DH, Makaroun MS, Nemoto EM, Ogawa S, et al. Association of intraluminal thrombus in abdominal aortic aneurysm with local hypoxia and wall weakening. J Vasc Surg 2001;34(2):291–9.
[14] Vorp D, Wang D, Webster M, Federspiel W. Effect of intraluminal thrombus thickness and bulge diameter on the oxygen diffusion in abdominal aortic aneurysm. J Biomech Eng 1998;120(5):579–83.
[15] Vorp DA, Geest JPV. Biomechanical determinants of abdominal aortic aneurysm rupture. Arterioscler, Thromb, Vasc Biol 2005;25(8):1558–66.
[16] Sun N, Leung JH, Wood NB, Hughes AD, Thom SA, Cheshire NJ, et al. Computational analysis of oxygen transport in a patient-specific model of abdominal aortic aneurysm with intraluminal thrombus. Br J Radio 2009:S18–23.
[17] Zakerzadeh R, Cupac T, Dorfner N, Guy A. Coupled hemodynamics and oxygen diffusion in abdominal aortic aneurysm: a computational sensitivity study. Cardiovasc Eng Technol 2021;12(2):166–82.
[18] Throop A, Bukac M, Zakerzadeh R. Prediction of wall stress and oxygen flow in patient-specific abdominal aortic aneurysms: the role of intraluminal thrombus. Biomech Model Mechanobiol 2022:1–19.
[19] Carbino B, Guy A, Durka M, Zakerzadeh R. The effects of geometric features of intraluminal thrombus on the vessel wall oxygen deprivation. Front Bioeng Biotechnol 2022;10:814995.
[20] Zakerzadeh R, Cupac T, Durka M. Oxygen transport in a permeable model of abdominal aortic aneurysm. Comput Methods Biomech Biomed Eng 2020:1–15.
[21] Throop A, Badr D, Durka M, Bukač M, Zakerzadeh R. Analyzing the effects of multi-layered porous intraluminal thrombus on oxygen flow in abdominal aortic aneurysms. Oxygen 2022;2(4):518–36.
[22] Polzer S, Gasser TC, Markert B, Bursa J, Skacel P. Impact of poroelasticity of intraluminal thrombus on wall stress of abdominal aortic aneurysms. Biomed Eng OnLine 2012;11. 62-62.
[23] Ayyalasomayajula A, Vande Geest JP, Simon BR. Porohyperelastic finite element modeling of abdominal aortic aneurysms. J Biomech Eng 2010;132(10):104502.
[24] Raptis A, Xenos M, Dimas S, Giannoukas A, Labropoulos N, Bluestein D, et al. Effect of macroscale formation of intraluminal thrombus on blood flow in abdominal aortic aneurysms. Comput Methods Biomech Biomed Engin 2016;19(1):84–92.
[25] Di Martino ES, Vorp DA. Effect of variation in intraluminal thrombus constitutive properties on abdominal aortic aneurysm wall stress. Ann Biomed Eng 2003;31(7):804–9.
[26] Sano M, Unno N, Sasaki T, Baba S, Sugisawa R, Tanaka H, et al. Topologic distributions of vasa vasorum and lymphatic vasa vasorum in the aortic adventitia–implications for the prevalence of aortic diseases. Atherosclerosis 2016;247:127–34.
[27] Wolinsky H, Glagov S. Nature of species differences in the medial distribution of aortic vasa vasorum in mammals. Circ Res 1967;20(4):409–21.
[28] Blassova T, Tonar Z, Tomasek P, Hosek P, Hollan I, Treska V, et al. Inflammatory cell infiltrates, hypoxia, vascularization, pentraxin 3 and osteoprotegerin in abdominal aortic aneurysms–a quantitative histological study. PloS One 2019;14(11):e0224818.
[29] Phillippi JA. On vasa vasorum: a history of advances in understanding the vessels of vessels. Sci Adv 2022;8(16):eabl6364.
[30] Tanaka H, Zaima N, Sasaki T, Sano M, Yamamoto N, Saito T, et al. Hypoperfusion of the adventitial vasa vasorum develops an abdominal aortic aneurysm. PLoS One 2015;10:8.

[31] Olsen PS, Schroeder T, Agerskov K, Røder O, Sørensen S, Perko M, et al. Surgery for abdominal aortic aneurysms. A survey of 656 patients. J Cardiovasc Surg 1991;32 (5):636–42.
[32] Kugo H, Zaima N, Tanaka H, Hashimoto K, Miyamoto C, Sawaragi A, et al. Pathological analysis of the ruptured vascular wall of hypoperfusion-induced abdominal aortic aneurysm animal model. J Oleo Sci 2017;66(5):499–506.
[33] Kugo H, Sukketsiri W, Tanaka H, Fujishima R, Moriyama T, Zaima N. Time-dependent pathological changes in hypoperfusion-induced abdominal aortic aneurysm. Biology 2021;10(2):149.
[34] Tanaka H, Unno N, Yata T, Kugo H, Zaima N, Sasaki T, et al. Creation of a rodent model of abdominal aortic aneurysm by blocking adventitial vasa vasorum perfusion. JoVE (J Vis Exp) 2017;129:e55763.
[35] Updegrove A, Wilson NM, Merkow J, Lan H, Marsden AL, Shadden SC. SimVascular: an open source pipeline for cardiovascular simulation. Ann Biomed Eng 2017;45(3):525–41.
[36] Ballyk P, Steinman D, Ethier C. Simulation of non-Newtonian blood flow in an end-to-side anastomosis. Biorheology 1994;31(5):565–86.
[37] Perktold K, Peter RO, Resch M, Langs G. Pulsatile non-Newtonian blood flow in three-dimensional carotid bifurcation models: a numerical study of flow phenomena under different bifurcation angles. J Biomed Eng 1991;13(6):507–15.
[38] Liu X, Fan Y, Deng X, Zhan F. Effect of non-Newtonian and pulsatile blood flow on mass transport in the human aorta. J Biomech 2011;44(6):1123–31.
[39] Fournier RL. Basic transport phenomena in biomedical engineering. CRC Press; 2017.
[40] Ma P, Li X, Ku DN. Heat and mass transfer in a separated flow region for high Prandtl and Schmidt numbers under pulsatile conditions. Int J Heat Mass Transf 1994;37(17):2723–36.
[41] Iannetti L, D'Urso G, Conoscenti G, Cutri E, Tuan RS, Raimondi MT, et al. Distributed and Lumped Parameter Models for the Characterization of High Throughput Bioreactors. PLoS One 2016;11(9):e0162774.
[42] Vosse FN. v.d. and N. Stergiopulos, Pulse Wave Propagation in the Arterial Tree. Annu Rev Fluid Mech 2011;43(1):467–99.
[43] Cheng CP, Taylor CA, Dalman RL. Abdominal aortic hemodynamics in intermittent claudication patients at rest and during dynamic pedaling exercise. Ann Vasc Surg 2015;29(8):1516–23.
[44] Les AS, Yeung JJ, Schultz GM, Herfkens RJ, Dalman RL, Taylor CA. Supraceliac and infrarenal aortic flow in patients with abdominal aortic aneurysms: mean flows, waveforms, and allometric scaling relationships. Cardiovasc Eng Technol 2010;1: 39–51.
[45] Ku DN. Blood flow in arteries. Annu Rev Fluid Mech 1997;29(1):399–434.
[46] Ansys, I., *ANSYS CFX-Solver Theory Guide Release 2020-R1*. 2020, ANSYS, Inc. Canonsburg, PA, USA.
[47] Geuzaine C, Remacle JF. Gmsh: A 3–D finite element mesh generator with built-in pre-and post-processing facilities. Int J Numer Methods Eng 2009;79(11):1309–31.
[48] Bukač M, Shadden SC. Quantifying the effects of intraluminal thrombi and their poroelastic properties on abdominal aortic aneurysms. Arch Appl Mech 2021:1–12.
[49] Kemmerling EMC, Peattie RA. Abdominal aortic aneurysm pathomechanics: current understanding and future directions. Adv Exp Med Biol 2018;1097:157–79.
[50] Buerk DG, Goldstick TK. Arterial wall oxygen consumption rate varies spatially. Am J Physiol-Heart Circ Physiol 1982;243(6):H948–58.
[51] Buerk DG, Goldstick TK. Oxygen tension changes in the outer vascular wall supplied by vasa vasorum following adenosine and epinephrine. J Vasc Res 1986; 23(1):9–21.
[52] Swillens Al, Lanoye L, Backer JD, Stergiopulos N, Verdonck PR, Vermassen F, et al. Effect of an abdominal aortic aneurysm on wave reflection in the aorta. IEEE Trans Biomed Eng 2008;55:1602–11.
[53] Fraser KH, Meagher S, Blake JR, Easson WJ, Hoskins PR. Characterization of an abdominal aortic velocity waveform in patients with abdominal aortic aneurysm. Ultrasound Med Biol 2008;34(1):73–80.
[54] Kolandavel MK, Fruend ET, Ringgaard S, Walker PG. The effects of time varying curvature on species transport in coronary arteries. Ann Biomed Eng 2006;34(12): 1820–32.
[55] Peattie RA, Schrader T, Bluth EI, Comstock CE. Development of turbulence in steady flow through models of abdominal aortic aneurysms. J Ultrasound Med 1994;13(6):467–72.
[56] Rappitsch G, Perktold K. Computer simulation of convective diffusion processes in large arteries. J Biomech 1996;29(2):207–15.
[57] Moore JA, Ethier CR. Oxygen mass transfer calculations in large arteries. J Biomech Eng 1997;119(4):469–75.